ELSEVIER

Journal of Nuclear Materials 279 (2000) 317–329

journal of nuclear materials

www.elsevier.nl/locate/jnucmat

Analysis of constituent redistribution in the γ (bcc) U–Pu–Zr alloys under gradients of temperature and concentrations

Y.H. Sohn [a,1], M.A. Dayananda [a,*], G.L. Hofman [b], R.V. Strain [b], S.L. Hayes [c]

[a] *School of Materials Engineering, Purdue University, 1289 MSEE Building, West Lafayette, IN 47907-1289, USA*
[b] *Argonne National Laboratory, 9700 South Cass Avenue, Argonne, IL 60439, USA*
[c] *Argonne National Laboratory, Idaho Falls, ID 83403-2528, USA*

Received 4 May 1999; accepted 30 November 1999

Abstract

Rods of a ternary alloy (71U–19Pu–10Zr by weight percent) were annealed under a temperature gradient of 220°C/cm for 41 days and examined for micro-structural development and compositional redistribution. An enrichment of Zr with concurrent depletion of U was observed within the γ (bcc) phase region on the hot-end side ($T \cong 740$°C). The experimental redistribution of the elements in the γ (bcc) phase was analyzed in the framework of multicomponent mass transport with due consideration of thermotransport and ternary diffusional interactions. Based on a new analysis involving an integration of interdiffusion fluxes in the diffusion zone, kinetic parameters related to the thermotransport and ternary interdiffusion were calculated for each component i over selected ranges of composition. The thermotransport coefficients of U, Pu, and Zr were in the approximate ratio of 1:2:−4.5 in the hot-end region. In addition, the interdiffusion flux contributions arising from the gradients of temperature and concentrations of U and Zr were estimated.

1. Introduction

The phenomenon of thermotransport or thermomigration refers to the constituent redistribution that occurs in a material in the presence of a temperature gradient [1–6]. Fuels and supporting structural materials in nuclear reactors are subject to appreciable temperature gradient and the redistribution of elements due to thermomigration can result in changes in physical and mechanical properties of alloys [1–6]. For metallic alloy fuels, such as U–Pu–Zr alloys, thermotransport during irradiation leads to variations in local power production, fission product generation and irradiation behavior such as swelling [7–12]. Most of the studies [13–22] related to thermotransport are generally limited to either a pure element, an interstitial binary alloy or a dilute binary substitutional solution. An experimental study of thermotransport utilizes the assumption of steady state for the fluxes or knowledge of interdiffusion coefficients for the determination of heats of transport from the redistribution of components under a temperature gradient.

In two experimental investigations of thermotransport in substitutional ternary U–Pu–Zr alloys reported in the literature [23,24], Zr enrichment has been observed in the colder regions. Kurata et al. [23] concluded that Zr migrated to the cold end ($T = 350$°C) of the alloy sample on the basis of α-autoradiography and electron microprobe (EMPA) analysis. However, the redistribution profiles presented by Kurata et al. [23] (Figs. 4 and 10 of their paper) clearly show that Zr also migrated with a concurrent depletion of U towards the hot end ($T = 850$°C) of the sample; this observation was ignored in their paper. Harbur et al. [24] have also reported Zr migration towards the colder regions of the U–Pu–Zr alloy in their thermotransport experiments carried out for the annealing time of 400 h; their observation was

* Corresponding author. Tel.: +1-765 494 4113; fax: +1-765 494 1204.
E-mail address: dayanand@ecn.purdue.edu (M.A. Dayananda).
[1] Present address: Department of Metallurgy and Materials Engineering, Institute of Materials Science, University of Connecticut, 97 North Eagleville Road, U-136, Storrs, CT 06269-3136, USA.

0022-3115/00/$ - see front matter
PII: S0022-3115(99)00290-1

based on differences of only 1–2 wt% in composition determined only at a few locations in the sample. Several attempts have also been made to model the redistribution of Zr and U by numerical analyses on the basis of approximate thermodynamic and kinetic coefficients [7–12,25,26], and these models are limited as they ignore ternary diffusional interactions under multiple concentration gradients and lack information on kinetic parameters associated with thermotransport.

In this study, rods of a ternary U–Pu–Zr alloy were annealed under a controlled temperature gradient and examined for micro-structural and compositional variations. The redistribution of the components experimentally observed are examined in the broad framework of multicomponent diffusion where interdiffusion fluxes are expressed in terms of a temperature gradient and two independent gradients of concentrations. An analysis developed [27] for the determination of average interdiffusion coefficients over selected composition ranges of an isothermal diffusion couple has been extended in this study to ternary diffusion under a temperature gradient. The analysis employs an integration of fluxes over selected regions of the diffusion zone and employs the concepts of average effective interdiffusion coefficients and average thermotransport coefficients for the individual components. These coefficients are determined from an application of the analysis to the concentration profiles of the U–Pu–Zr rods. In addition, ternary interdiffusion coefficients are evaluated for selected regions in the diffusion zone and the diffusion flux contributions arising from the gradients of temperature and concentrations are estimated.

2. Experimental

The samples were cut from an injection-cast cylindrical rod that had a diameter of 5.7 mm, a length of 63.5 mm and the nominal composition of 71U–19Pu–10Zr by weight percent. Chemical analyses of sections adjacent to the samples used in the present experiment showed that their compositions were within 0.5 wt% of the nominal composition. The samples were ground by using SiC papers to provide flat ends that were perpendicular to the longitudinal axis. The samples were then sealed in a stainless steel chamber situated at one end of a stainless rod that fitted in a furnace. The hot end of the samples was separated from the stainless steel rod by a tungsten disc to prevent interaction between the U–Pu–Zr alloy and the stainless steel. To ensure good contacts and heat transfer, the samples were placed in slight compression by fitting a copper rod to the other end of the sample. The copper rod was cooled by circulating water at 25°C to maintain one end of the sample cold.

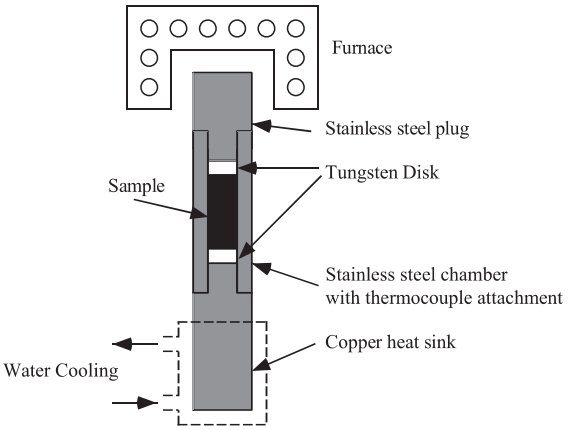

Fig. 1. Schematic illustration of the sample-holder assembly and setup for thermotransport experiments.

Thermocouples were laser welded into the wall of the sample chamber at locations corresponding to the two ends and mid-length of the samples. The entire assembly was placed in an insulating shell to minimize radial temperature gradients in the samples and positioned in a glove box as shown in Fig. 1. Similar experimental setup has been used to study the redistribution of Pu and U in mixed oxide fuel materials in a thermal gradient [28]. The furnace temperature was controlled by a separate thermocouple. The sample thermocouple readings were recorded on a strip chart and had a maximum variation of ± 5°C over the duration of an experiment. The annealing experiment was terminated by switching off the power and by maintaining the cooling of the copper rod in contact with the sample with circulating water. Upon the completion of the experiments, each sample was mounted longitudinally, ground and polished to its centerline for metallographic and compositional analysis.

Two samples, designated A and B, were employed for the thermotransport experiments and the test parameters are given in Table 1. In addition, two samples, identified by C and D, were isothermally annealed at 750°C and 650°C, respectively; the isothermal experi-

Table 1
Thermotransport and isothermal diffusion experiments with U–19Pu–10Zr (wt%) alloy

Specimen[a] designation	Temperature range (°C)	Test duration (h)
A	600–740	984
B	615–750	2736
C	750 (Isothermal)	10
D	650 (Isothermal)	10

[a] Specimen nominal dimensions: 63.5 mm in length by 5.7 mm in diameter.

ments helped compare and verify alloy microstructures developed in the non-isothermal experiments and examine any surface effects on the constituent redistribution under a temperature gradient. All samples were examined for semi-quantitative compositional data with a scanning electron microscope (SEM) equipped with an energy dispersive spectrometer (EDS). The redistribution of constituents in sample A was determined quantitatively by EMPA along two parallel traces near the longitudinal centerline of the sample. Sample B was examined for light elements by scanning auger microscopy (SAM).

3. Microstructural and compositional development

3.1. Microstructural observations

The U–Pu–Zr alloy consists of the bcc solid solution of the γ phase in the temperature range 650–750°C. This is confirmed by the neutron diffraction patterns [29] shown in Fig. 2. The γ (bcc) phase exists down to about 600°C in a two-phase mixture with the ζ (tetragonal) phase. Below 600°C, the γ phase transforms to the δ (hexagonal) phase; the familiar intermediate U–Zr phase with an extensive solid solubility for Pu. Below 500°C, the ζ phase rejects the α (orthorhombic) phase, a U–Pu solid solution. These results of the neutron diffraction patterns correspond well to the ternary isotherms of the U–Pu–Zr system [30].

The room temperature microstructures of samples C and D isothermally annealed at 750°C and 650°C are presented in Fig. 3. The microstructures of samples C and D consist of ζ (white) and δ (dark) phases, indicating that the bcc γ phase cannot be retained upon cooling. For these samples, the ζ phase forms first at the original γ grain boundaries, followed by a decomposition of the γ phase into ζ and δ phases during cooling. The black, globular precipitates in the micrographs in Fig. 3 correspond to a Zr-rich phase containing N, O and C; they are commonly observed in U–Pu–Zr alloys and are considered to form during alloy preparation due to the interstitial impurities present in the feed stock.

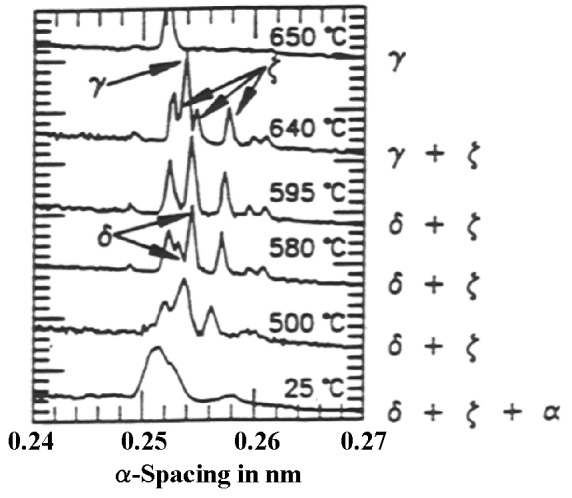

Fig. 2. Neutron diffraction patterns [29] for the U–19Pu–10Zr (wt%) alloys at various temperatures.

Microstructures of sample A subjected to a thermotransport experiment are presented in Fig. 4 for selected temperature locations; these microstructures are consistent with those presented in Fig. 3. For example, the microstructures presented in Figs. 3(a) and 4(a) for similar temperatures are comparable; also, microstructures in Figs. 3(c) and 4(b) are quite similar and correspond to similar temperatures.

In Fig. 5, microstructures are presented for sample A near the hot end. The microstructure in Fig. 5(a) shows the ζ phase formed at the prior γ grain boundaries, while that in Fig. 5(b) shows the formation of a (ζ + δ) two-phase mixture in the grain interior. The morphology of this two-phase structure is, however, much finer and has a larger fraction of the δ phase than that observed for the isothermally annealed sample shown in Fig. 3(b). In Fig. 6 is presented a microstructure with qualitative information on the build-up of Zr in the hot-end region of sample A. The increased Zr content is consistent with the larger fraction of the δ phase mentioned above. Another important observation is the formation of a Zr-rich layer at the hot surface of all samples as identified in Fig. 7. This layer contained approximately 80 wt% Zr with O, N and C and was similar in composition to the globular Zr precipitates observed in Fig. 3. From Fig. 7 it is apparent that the formation of the Zr-rich layer is not a result of the temperature gradient, as it is also observed in the isothermally annealed samples. Its formation is likely due to the reaction of Zr with impurities present in the encapsulating materials. In the isothermally annealed samples, the layer formation resulted in Zr depletion in the alloy over a depth of about 10 μm, as shown in Fig. 7(c) on the basis of EDS analysis. The Zr-rich layer did not increase in thickness for annealing times beyond 10 h and indicated adequate depletion of the impurities responsible for its formation. Such a Zr-depleted region was not observed in the samples annealed under a thermal gradient due to an overcompensating migration of Zr towards the hot end.

3.2. Redistribution of constituents

The redistribution of U, Pu and Zr constituents was examined initially by semi-quantitative EDS analysis.

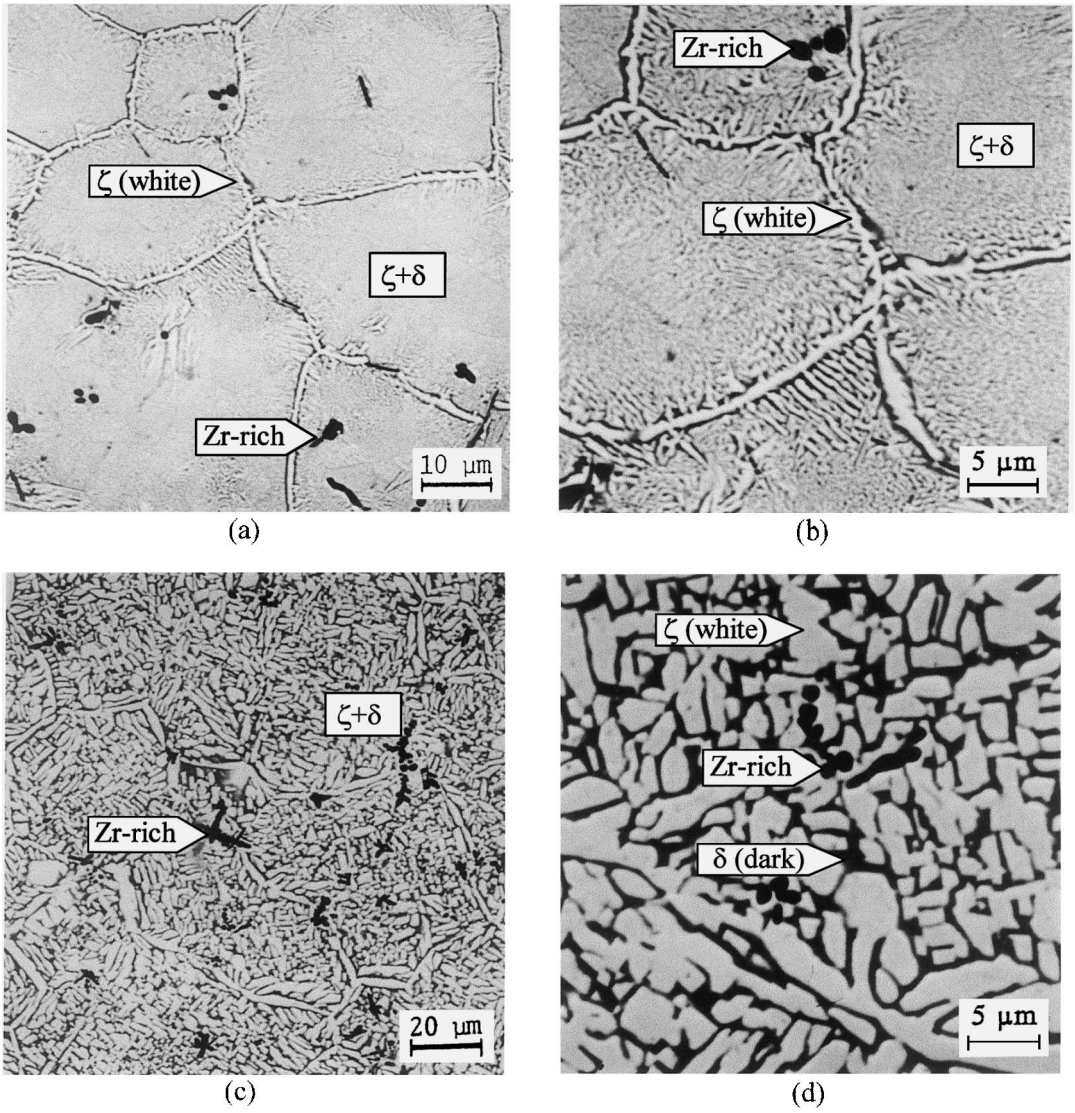

Fig. 3. Backscattered electron micrographs showing the microstructures (a) and (b) of sample C and (c) and (d) of sample D. Samples C and D were isothermally annealed at 750°C and 650°C, respectively, for 10 h.

Since multiphase micro-structural regions were observed, the variation in the composition across the sample was evaluated by using a relatively large electron beam size and the EDS measurements presented in Fig. 8 show the redistribution profiles of U, Pu and Zr for samples A and B. An enrichment of Zr along with a depletion of U is evident near the hot end ($x = 0$ μm) of the samples and the concentration of Pu changes very little. If one assumes a linear temperature gradient in the samples A and B, then the changes in the composition can be presumed to occur well within the γ phase over the temperature range 650–750°C. Furthermore, the observed multiphase microstructures at room temperature are consistent with the redistribution profiles presented in Fig. 8. Thus, the changes in composition in samples A and B under the temperature gradient need to be understood in terms of both the thermotransport in the γ phase and the concurrent interdiffusion of the components driven by concentration gradients.

The concentration profiles determined near the cold end ($x = 6350$ μm) of the samples in Fig. 8 show an increase in Zr content and a decrease in U. Such variations suggest transport opposite to that observed near the hot end of the samples. The cold end of sample consisted of δ and α phases at room temperature indicating the

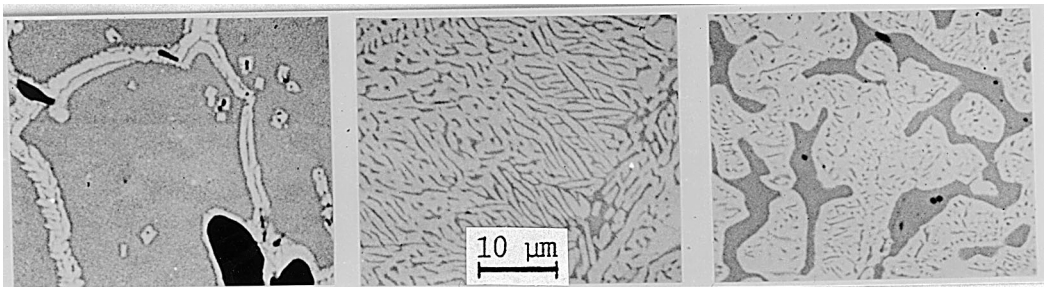

Fig. 4. Backscattered electron micrographs of the U–Pu–Zr alloy sample A after the thermotransport experiment: (a) near hot end ($T_{hot} \approx 740$°C), (b) mid-length ($T_{mid} \approx 670$°C) and (c) near cold end ($T_{cold} \approx 600$°C). In micrograph (a), white and black regions correspond to ζ and Zr-rich phases, respectively; gray region represents fine mixture of α and δ phases. In (b) and (c), the white and gray regions correspond to α and δ phases, respectively.

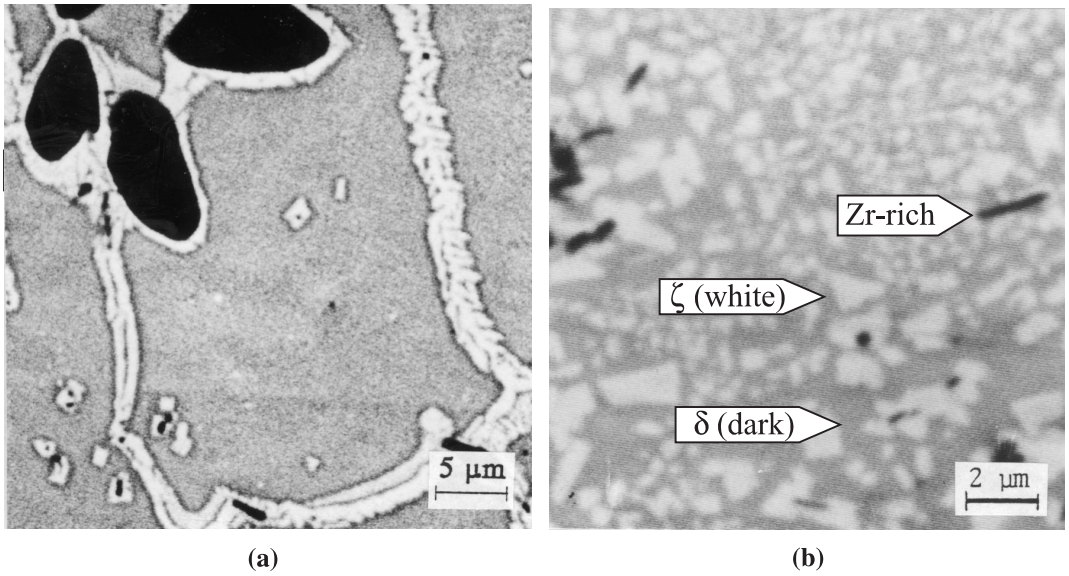

Fig. 5. Backscattered electron micrographs showing the microstructure of the U–Pu–Zr alloy sample A near the hot end after the thermotransport experiment: (a) the ζ (white) phase forms at the prior γ grain boundaries and (b) in the grain interior with much finer morphology.

presence of δ and ζ phases during the thermotransport anneal. An understanding of the redistribution of the constituents in a multiphase region requires a knowledge of ternary thermodynamic data for the individual phases, specifically the molar heat of mixing [31] and such data are not available. The kinetic analysis carried out in this study is limited to the γ phase. For the kinetic analysis carried out in this study, concentration profiles of U, Pu and Zr were determined by EMPA analysis for sample A which was annealed under temperature gradient for 41 days. Elemental standards of U, Pu and Zr and ZAF correction were employed for quantitative determination of concentrations.

4. Determination of fluxes and diffusion parameters in the γ (bcc) phase

The experimental concentration profiles of U, Pu and Zr determined by EMPA in the γ (bcc) region of the sample A were curve-fitted by polynomial expressions. The interdiffusion flux of each component was determined directly from the concentration profile on the basis of a laboratory-fixed reference frame [32–36]. From an integration of the interdiffusion fluxes over the diffusion zone, an average thermotransport coefficient and an average effective interdiffusion coefficient are defined for each component and determined over

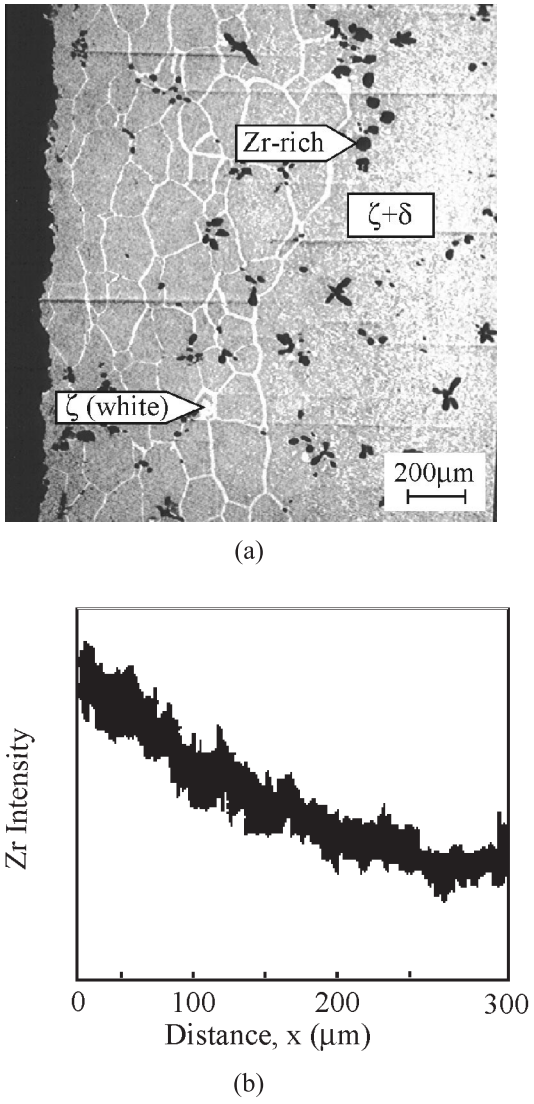

Fig. 6. (a) Backscattered electron micrographs showing the microstructural variations near the hot end and (b) the variation in Zr concentration determined by EMPA.

selected regions in the diffusion zone. These diffusion parameters are also determined at locations where concentration profiles exhibit a relative maximum or a relative minimum and at locations of zero flux planes (ZFPs) [32–36].

4.1. Determination of interdiffusion fluxes

A laboratory-fixed frame of reference was employed for the determination of fluxes of all components. Fig. 9 represents a schematic concentration profile of Zr in the γ phase and the surface layer consisting mostly of Zr. The origin x_0 of the laboratory-fixed reference frame is identified at $x = 0$ on the basis of mass balance requirement expressed by: area S = area (A − B − C). For specimen A (984 h anneal with $dT/dx = 220.5°C/cm^{-1}$), x_0 was identified at $x = 0$ based on mass balance from the concentration profiles of the components shown in Fig. 10(a). The mass balance for Zr included the 20-μm thick Zr-rich layer (containing approximately 80% Zr) observed at the surface maintained at the high temperature (740°C).

With the assumption that the concentration C_i is a function of the Boltzmann parameter $(x - x_0)/\sqrt{t}$, the interdiffusion flux $\tilde{J}_i$ for component i at time t can be calculated from the relation [32–36]

$$\tilde{J}_i = \frac{1}{2t}\int_{C_i^I}^{C_i^0} (x - x_0)\,dC_i \quad (i = 1, 2, \ldots, n). \tag{1}$$

In Fig. 9 is presented a schematic concentration profile identifying the concentration C_i^I of component i in the two-phase $(\gamma + \zeta)$ region and the concentration C_i^0 of component i at x_0 identified $x = 0$. For the calculation of the interdiffusion fluxes, the concentration C_i^I of component i in the two-phase $(\gamma + \zeta)$ region is assumed to vary little from the initial alloy concentration. Also, the concentration C_i^0 at $x = 0$ is assumed to get setup early in the experiment and remain unchanged over time. Under these conditions, the location x of a concentration level C_i varies parabolically with time t.

The curve-fitted experimental concentration profiles of U, Pu and Zr for sample A are presented in Fig. 10(a). On the basis of Eq. (1), the interdiffusion fluxes of U, Pu and Zr were calculated from these concentration profiles and are presented in Fig. 10(b). The interdiffusion fluxes for U and Pu are largely positive and that for Zr is largely negative. Also, ZFPs [32–36] were observed for the various components at sections identified by $x = 3600$ μm for U, $x = 3800$ μm for Pu, $x = 3750$ μm for Zr. At a ZFP, the interdiffusion flux of a component goes to zero and shows a change or reversal in its direction on either side of the ZFP [32–36]. For example, Fig. 10 shows that the interdiffusion flux of Zr is in the negative direction (up the concentration gradient) to the left of its ZFP, as opposed to the positive direction (down the concentration gradient) to the right of ZFP.

4.2. Calculation of diffusion parameters

An analysis [27] utilizing an integration of interdiffusion fluxes has been recently developed to determine average ternary interdiffusion coefficients over selected composition ranges of an isothermal diffusion couple. This analysis can be extended and applied to examine ternary interdiffusion under a temperature gradient.

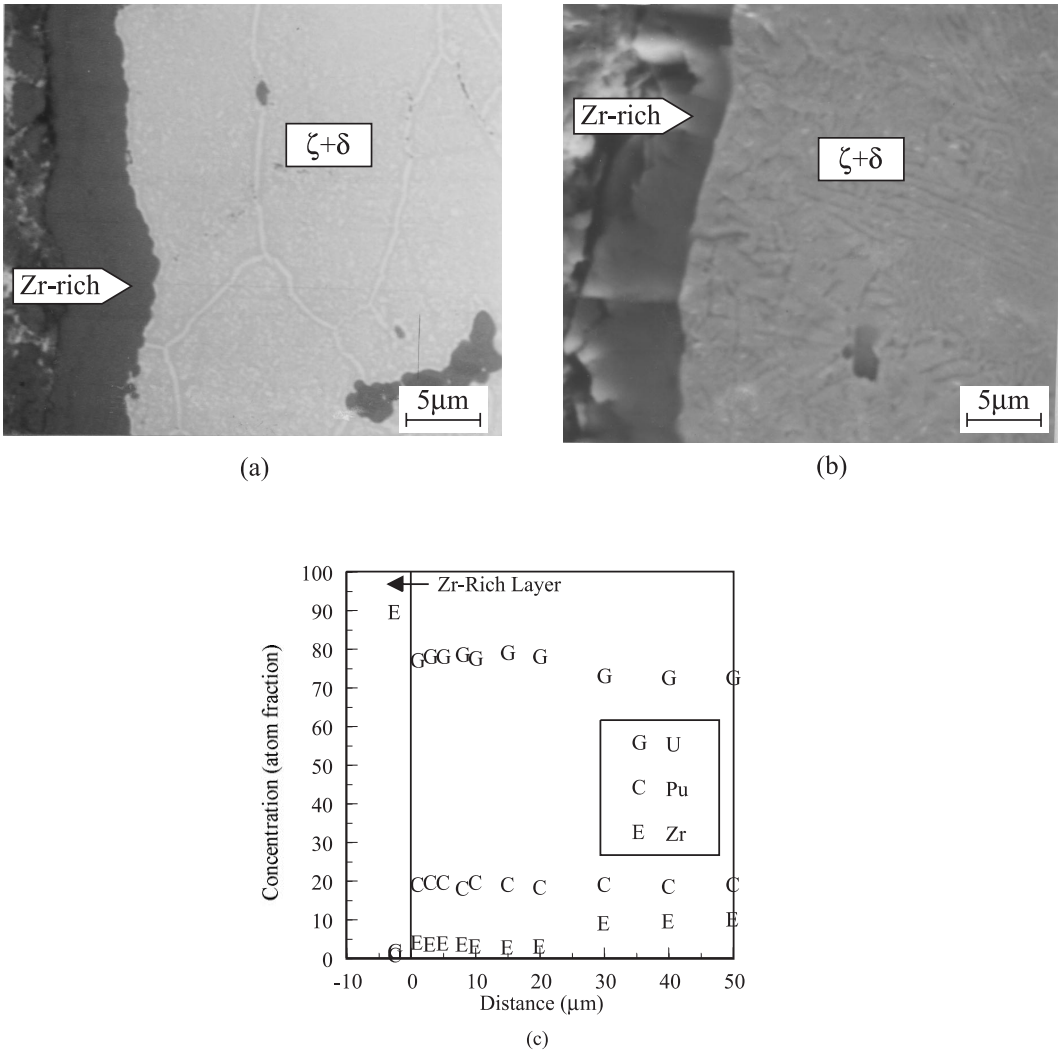

Fig. 7. Zr-rich layer (dark) formed: (a) at the hot surface of sample A annealed under a temperature gradient, (b) at the surface of sample D annealed isothermally at 750°C and (c) the concentration profiles of U, Pu and Zr determined by EDS for isothermally annealed sample D do not exhibit any significant diffusion of constituents.

For non-isothermal diffusion in a ternary system, the interdiffusion flux of component i can be related to the gradients of temperature $\partial T/\partial x$ and concentrations $\partial C_j/\partial x$ by [6]

$$\tilde{J}_i = -C_i\beta_i\tilde{Q}_i^*\frac{1}{T}\frac{\partial T}{\partial x} - \sum_{j=1}^{2}\tilde{D}_{ij}^3\frac{\partial C_j}{\partial x} \quad (i=1,2), \tag{2}$$

where β_i is the mobility and $\tilde{Q}_i^*$ the heat of transport for component i. The $\tilde{D}_{ij}^3$ coefficients refer to the four concentration-dependent ternary interdiffusion coefficients. Over a selected range x_1–x_2 of the concentration profile, the interdiffusion flux $\tilde{J}_i$ can be integrated to yield

$$\int_{x_1}^{x_2}\tilde{J}_i\,\mathrm{d}x = -\overline{\beta_i\tilde{Q}_i^*}\int_{T(x_1)}^{T(x_2)}C_i\frac{\mathrm{d}T}{T} - \overline{\tilde{D}}_i^{\mathrm{eff}} \times \int_{C(x_1)}^{C(x_2)}\mathrm{d}C_i \quad (i=1,2), \tag{3}$$

where $\overline{\beta_i\tilde{Q}_i^*}$ is defined as the average thermotransport coefficient and $\overline{\tilde{D}}_i^{\mathrm{eff}}$ as the average effective interdiffusion coefficient for component i. $\overline{\tilde{D}}_i^{\mathrm{eff}}$ over a concentration range ΔC_i is related to the average main and cross interdiffusion coefficients by Dayananda and Coworkers [37–40]

$$\overline{\tilde{D}}_i^{\mathrm{eff}} = \overline{\tilde{D}}_{ii}^3 + \overline{\tilde{D}}_{ij}^3\frac{\Delta C_j}{\Delta C_i} \quad (i\neq j). \tag{4}$$

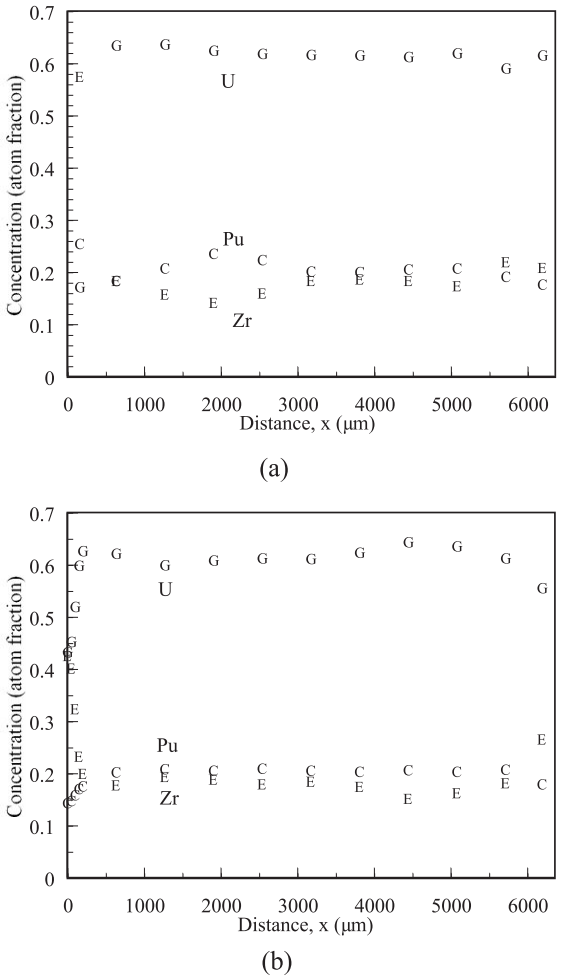

Fig. 8. Constituent redistribution profiles of U, Pu and Zr under the temperature gradient for: (a) sample A and (b) sample B evaluated by EDS analysis.

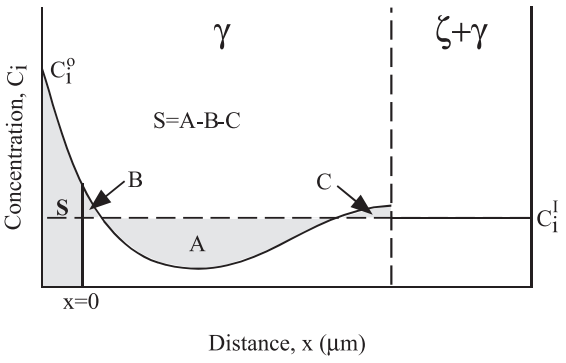

Fig. 9. A schematic of concentration profile for Zr developed in the diffusion zone. A laboratory-fixed frame of reference was determined on the basis of concentration profiles when area S = area (A – B – C).

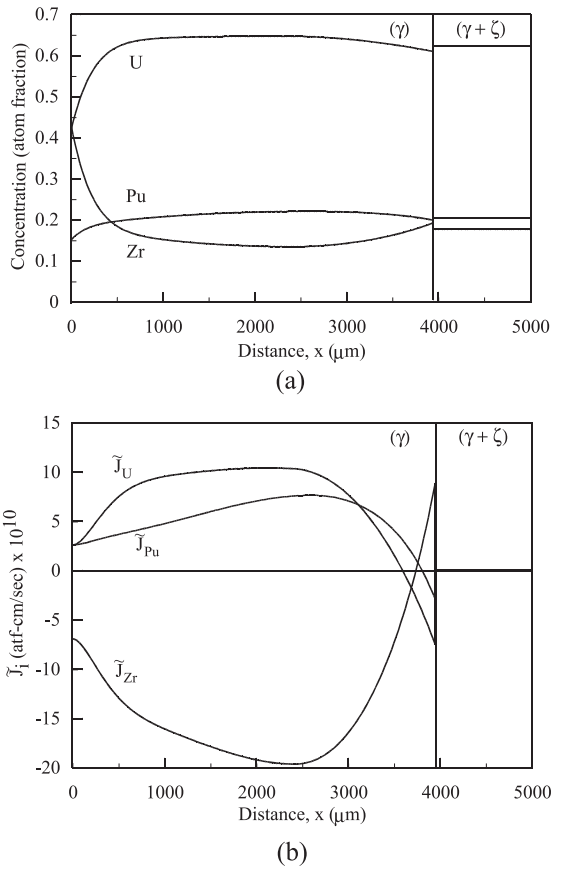

Fig. 10. (a) Experimental concentration profiles determined by EMPA and (b) the corresponding interdiffusion flux profiles for U, Pu and Zr in the γ phase under the gradients of temperature and concentrations.

Another expression involving an integration of $\tilde{J}_i x$ over x_1–x_2 can be written as

$$\int_{x_1}^{x_2} \tilde{J}_i(x-x_0)\,\mathrm{d}x = -\overline{\beta_i \tilde{Q}_i^*} \int_{T(x_1)}^{T(x_2)} C_i \frac{(x-x_0)\,\mathrm{d}T}{T} - \overline{\tilde{D}}_i^{\mathrm{eff}} \int_{C(x_1)}^{C(x_2)} (x-x_0)\,\mathrm{d}C_i \quad (i=1,2). \tag{5}$$

Eqs. (3) and (5) provide two equations for the determination of $\overline{\beta_i \tilde{Q}_i^*}$ and $\overline{\tilde{D}}_i^{\mathrm{eff}}$ for each component over any selected region. By using the interdiffusion flux profiles shown in Fig. 10(b), Eqs. (3) and (5) were simultaneously solved to determine the diffusion parameters for each component in three selected regions within the γ phase; the calculated parameters are presented in Table 2. The regions selected are identified as region I from 0 to 1000 μm, region II from 1000 to 2450 μm, and region III from 2450 to 3950 μm.

Table 2
Diffusion parameters, $\overline{\beta_i\tilde{Q}_i^*}$, $\overline{\tilde{Q}_i^*}$ and $\overline{\tilde{D}_i^{\text{eff}}}$ calculated from the redistribution of U, Pu and Zr under the gradients of temperature and concentrations[a]

Region in the γ phase	Location (μm)	$\overline{\beta_i\tilde{Q}_i^*}$ (10^{-12} m^2/s)			$\overline{\tilde{Q}_i^*}$ (10^{-20} J)			$\overline{\tilde{D}_i^{\text{eff}}}$ (10^{-14} m^2/s)		
		U	Pu	Zr	U	Pu	Zr	U	Pu	Zr
I	0–1000	0.7	1.2	−5.5	0.7	0.6	−11.0	0.8	0.9	4.5
II	1000–2450	0.7	1.7	−6.8	0.7	0.9	−13.6	4.4	19.3	26.7
$\frac{\partial C_j}{\partial x}=0$	2125 for U, 2600 for Pu, 2425 for Zr	0.7	1.5	−6.4	0.7	0.8	−12.8	na	na	na
III	2450–4015	1.1	1.7	−8.6	1.1	0.9	−17.2	−47.8	−24.6	−51.3

[a] Note: $\overline{\tilde{Q}_i^*}$'s per atom were calculated on the basis of the estimated values [41] of $\overline{\beta}_U = 10\times10^{15}$ m^2/J s; $\overline{\beta}_{Pu}=20\times10^{15}$ m^2/J s; $\overline{\beta}_{Zr}=5\times10^{15}$ m^2/J s.

The calculated $\overline{\beta_i\tilde{Q}_i^*}$s for U and Pu in Table 2 are positive quantities and indicate that the heat of transport, $\tilde{Q}_i^*$s are positive (i.e., migration towards the cold end). Zr migrates towards the hot end on the basis of a negative $\overline{\beta_i\tilde{Q}_i^*}$. Table 2 shows that the values of $\overline{\beta_i\tilde{Q}_i^*}$ for each component vary little over the diffusion zone, while $\overline{\tilde{D}_i^{\text{eff}}}$ exhibits a change in sign and appreciable variation over different regions. From the β_i values reported for U–Pu–Zr alloys with similar compositions at 750°C [41], $\overline{\tilde{Q}_i^*}$ may be estimated; these are presented in Table 2.

At the locations where the concentration profile of a component exhibits a relative maximum or a relative minimum ($\partial C_j/\partial x = 0$), a substitution of Eq. (4) into Eq. (2) with further simplification yields

$$\tilde{J}_i = -C_i\beta_i\tilde{Q}_i^*\frac{1}{T}\frac{\partial T}{\partial x}. \tag{6}$$

In Fig. 10(a), these locations are at $x = 2125$ μm for U, $x = 2600$ μm for Pu, and $x = 2425$ μm for Zr. The product of mobility and heat of transport $\beta_i\tilde{Q}_i^*$ calculated from Eq. (6) for the components are reported in Table 2. There is good agreement between the $\beta_i\tilde{Q}_i^*$ values calculated from Eq. (6) and the $\overline{\beta_i\tilde{Q}_i^*}$ values determined from the simultaneous solution of Eqs. (3) and (5) in the region where a relative maximum or minimum in concentration is observed.

4.3. Zero flux planes

In the interdiffusion flux profiles shown in Fig. 10(b), ZFPs are observed for U, Pu and Zr at x values of 3600, 3800 and 3750 μm, respectively. At a ZFP, the interdiffusion flux of a component goes to zero and shows a change or reversal in its direction on either side of it [32–36]. According to Eq. (2), $\tilde{J}_i$ goes to zero for component i when the sum of the flux terms involving the temperature and concentration gradients equals zero. Then, at a ZFP Eq. (2) yields

Table 3
Comparison of the ratio $(\beta_i\tilde{Q}_i^*)/\tilde{D}_i^{\text{eff}}$ calculated from Eq. (9) at the ZFP and $(\overline{\beta_i\tilde{Q}_i^*})/\overline{\tilde{D}_i^{\text{eff}}}$ determined from a simultaneous solution of Eqs. (4) and (5) in the diffusion zone; the ZFP locations are: $x = 3600$ μm for U, $x = 3800$ μm for Pu, and $x = 3750$ μm for Zr

$(\beta_i\tilde{Q}_i^*)/\tilde{D}_i^{\text{eff}}$			$(\overline{\beta_i\tilde{Q}_i^*})/\overline{\tilde{D}_i^{\text{eff}}}$		
U	Pu	Zr	U	Pu	Zr
−2.4	−7.0	16.3	−2.2	−6.9	16.8

$$C_i\beta_i\tilde{Q}_i^*\frac{1}{T}\frac{\partial T}{\partial x} = -\tilde{D}_i^{\text{eff}}\frac{\partial C_i}{\partial x}, \tag{7}$$

where

$$\tilde{D}_i^{\text{eff}} = \tilde{D}_{ii}^k + \tilde{D}_{ij}^k\frac{\partial C_j}{\partial C_i}. \tag{8}$$

Hence, at the ZFP, the ratio $(\beta_i\tilde{Q}_i^*)/\tilde{D}_i^{\text{eff}}$ for a component can be determined by

$$\frac{\beta_i\tilde{Q}_i^*}{\tilde{D}_i^{\text{eff}}} = -\frac{(\partial C_i/\partial x)T}{(\partial T/\partial x)C_i}. \tag{9}$$

The ratios $(\beta_i\tilde{Q}_i^*)/\tilde{D}_i^{\text{eff}}$ calculated from Eq. (9) are reported in Table 3. The ratios of $(\overline{\beta_i\tilde{Q}_i^*})/\overline{\tilde{D}_i^{\text{eff}}}$ determined from the simultaneous solution of Eqs. (3) and (5) in region III, where the ZFP was observed, are also reported. Good agreement is observed between these two sets of ratios.

5. Estimation of flux contributions arising from various gradients

The calculated values of the average thermotransport coefficient $\overline{\beta_i\tilde{Q}_i^*}$ and the average effective interdiffusion

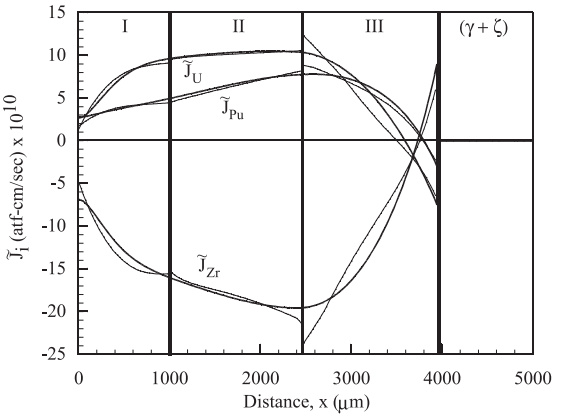

Fig. 11. Experimental (thick lines) and estimated (thin lines) interdiffusion flux profiles for the U–Pu–Zr alloy under gradients of temperature and concentrations. The experimental flux profiles, also shown in Fig. 10(b) are determined on the basis of Eq. (1). The estimated flux profiles were determined from Eqs. (2) and (4) with average coefficients of heat of transport $\overline{\beta_i \tilde{Q}_i^*}$ and average effective interdiffusion coefficient $\overline{\tilde{D}}_i^{\text{eff}}$ reported in Table 2.

coefficient $\overline{\tilde{D}}_i^{\text{eff}}$ presented in Table 2 were employed for estimating interdiffusion fluxes over selected regions of the diffusion zone on the basis of Eqs. (2) and (4). The estimated fluxes are shown in Fig. 11. The estimated interdiffusion fluxes for all components agree well with those originally calculated from Eq. (1).

From Eq. (4), $\overline{\tilde{D}}_i^{\text{eff}}$ is expressed in terms of the average main interdiffusion coefficient $\overline{\tilde{D}}_{ii}^{k}$ and the average cross interdiffusion coefficient $\overline{\tilde{D}}_{ij}^{k}$. Hence, Eqs. (2), (3) and (5), can be expressed by

$$\tilde{J}_i = -C_i \overline{\beta_i \tilde{Q}_i^*} \frac{1}{T} \frac{\partial T}{\partial x} - \overline{\tilde{D}}_{ii}^{k} \frac{\partial C_i}{\partial x} - \overline{\tilde{D}}_{ij}^{k} \frac{\partial C_j}{\partial x}, \tag{10}$$

$$\int_{x_1}^{x_2} \tilde{J}_i \, \mathrm{d}x = -\overline{\beta_i \tilde{Q}_i^*} \int_{T(x_1)}^{T(x_2)} C_i \frac{\mathrm{d}T}{T} - \overline{\tilde{D}}_{ii}^{k} \int_{C_i(x_1)}^{C_i(x_2)} \mathrm{d}C_i - \overline{\tilde{D}}_{ij}^{k} \int_{C_j(x_1)}^{C_j(x_2)} \mathrm{d}C_j \tag{11}$$

and

$$\int_{x_1}^{x_2} \tilde{J}_i (x - x_0) \, \mathrm{d}x = -\overline{\beta_i \tilde{Q}_i^*} \int_{T(x_1)}^{T(x_2)} C_i \frac{(x - x_0) \, \mathrm{d}T}{T} - \overline{\tilde{D}}_{ii}^{k} \int_{C_i(x_1)}^{C_i(x_2)} (x - x_0) \, \mathrm{d}C_i - \overline{\tilde{D}}_{ij}^{k} \times \int_{C_j(x_1)}^{C_j(x_2)} (x - x_0) \, \mathrm{d}C_j, \tag{12}$$

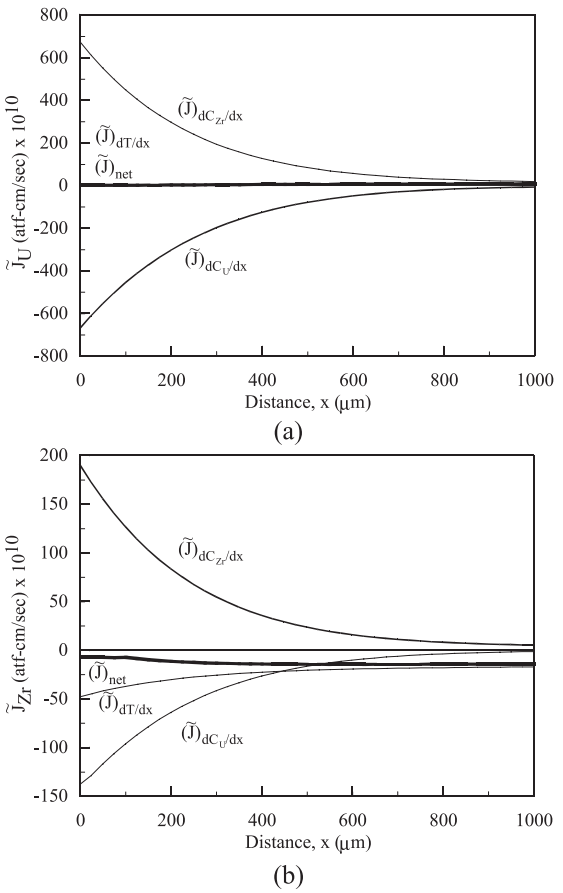

Fig. 12. Estimated contributions from the gradients of temperature and concentrations of U and Zr to the interdiffusion flux of: (a) U and (b) Zr in the region I (0–1000 μm).

respectively. Employing the $\overline{\beta_i \tilde{Q}_i^*}$ values reported in Table 2, Eqs. (11) and (12) were solved simultaneously to evaluate the average main interdiffusion coefficients $\overline{\tilde{D}}_{ii}^{k}$ and the average cross interdiffusion coefficients $\overline{\tilde{D}}_{ij}^{k}$ for Zr and U in the regions I and II; these coefficients are reported in Table 4. The cross interdiffusion coefficients are comparable in magnitude and sign to the average main interdiffusion coefficients and imply appreciable interactions between U and Zr during interdiffusion. This observation is consistent with similar findings of an earlier study on U–Pu–Zr isothermal diffusion at 750°C [42]. In region III, where $\overline{\tilde{D}}_i^{\text{eff}}$ is negative, the profiles of concentrations and interdiffusion fluxes were approximately linear and not conducive to the calculation of the main and cross coefficients [27].

From the calculated values of $\overline{\beta_i \tilde{Q}_i^*}$, $\overline{\tilde{D}}_{ii}^{k}$ and $\overline{\tilde{D}}_{ij}^{k}$, the flux contributions arising from the gradients of temperature, U concentration and Zr concentration were estimated in regions I and II and are presented in

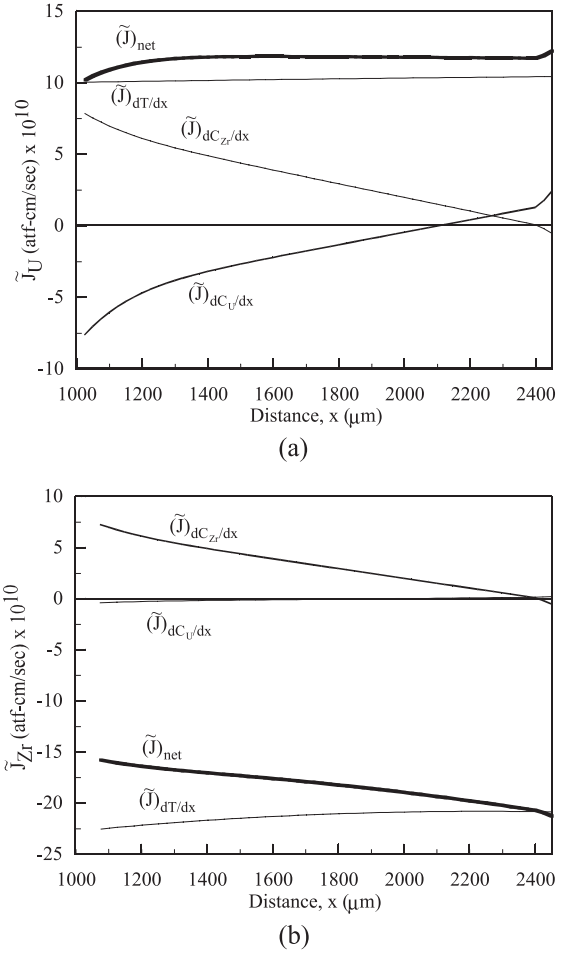

Fig. 13. Estimated contributions from the gradients of temperature and concentrations of U and Zr to the interdiffusion flux of: (a) U and (b) Zr in the region II (1000–2450 μm).

Figs. 12 and 13. The flux contributions corresponding to the three terms on the right-hand side of Eq. (10) are identified by $\tilde{J}_{i,\partial T/\partial x}$, $\tilde{J}_{i,\partial C_U/\partial x}$ and $\tilde{J}_{i,\partial C_{Zr}/\partial x}$ in Figs. 12 and 13. The magnitudes of flux contributions arising from the gradients of U and Zr are much greater than that of the flux due to the temperature gradient. However, the $\tilde{J}_{i,\partial C_U/\partial x}$ and $\tilde{J}_{i,\partial C_{Zr}/\partial x}$ terms are opposite in sign and their sum is quite small compared to $\tilde{J}_{i,\partial T/\partial x}$ as shown in Figs. 12 and 13.

Therefore, the constituent redistribution in the U–Pu–Zr alloy is brought about by both the temperature and concentration gradients. The flux contributions by the U and Zr gradients are similar in magnitudes but have opposite signs. The U migration to the colder regions of the sample is driven by both the gradients of temperature and Zr concentration. Similarly, the Zr migration to the hot end of the sample is driven by both the gradients of temperature and U concentration gradient in region I. In region II, the flux contribution due to the temperature gradient is generally larger in magnitude than that due to the concentration gradients. Therefore, it is concluded that both thermotransport as well as ternary diffusional interactions play important roles in contributing to the redistribution of elements in the γ phase region of the U–Pu–Zr system.

6. Comparison with previous experiments and post-irradiation observations

The present thermotransport experiment clearly exhibits a net transport of Zr in the γ phase to the hot end of the samples. Such observation has not been clearly brought out or emphasized in the earlier studies of thermotransport in U–Pu–Zr alloys [23,24]. The redistribution profiles presented by Kurata et al. [23] appear to indicate a Zr migration along with a depletion of U near the hot end (γ phase at $T = 850$°C) of their sample; however, the authors ignored this observation. In addition, it is unclear whether they employed in their experiments an inert barrier, like the tungsten disc, between the sample and the steel heating rod to prevent interdiffusion. The thermotransport experiment by Harbur et al. [24] was conducted for a relatively short time ~400 h; a small Zr enrichment of less that 1 wt% was observed at the cold end along with a small Zr depletion of less than 2 wt% at the mid-region ($T = 640$–680°C) of the sample. No observations were made on the redistribution of the elements in the hot end.

The migration of Zr to the hot regions of the U–Pu–Zr rods reported in this study is consistent with the available data for irradiated U–Pu–Zr fuels. In a large number of post-irradiation studies of U–Pu–Zr fuels, Zr consistently migrated [7,9,10] to the radial

Table 4
Average main and cross interdiffusion coefficients calculated from the experimental redistribution of U, Pu and Zr under gradients of temperature and concentrations

Region in the γ phase	$\overline{\tilde{D}^{Pu}_{UU}}$ (10^{-13} m^2/s)	$\overline{\tilde{D}^{Pu}_{UZr}}$ (10^{-13} m^2/s)	$\overline{\tilde{D}^{Pu}_{ZrU}}$ (10^{-13} m^2/s)	$\overline{\tilde{D}^{Pu}_{ZrZr}}$ (10^{-13} m^2/s)
I	7.5	6.0	1.6	1.7
II	7.0	2.9	0.5	2.9

center of the fuel pins up the temperature gradient, where the γ phase existed during irradiation and the temperature gradient was sufficiently large. Zr-migration down a temperature gradient has also been reported in colder axial positions along fuel pins where the radial center temperature was below the γ phase transitional temperature [7,9,10,23,24]. Such a migration of Zr at the colder end of the alloy rod is consistent with the present study as shown in Fig. 8. Appreciable changes in the relative amounts of δ and ζ phases may be expected with decrease in temperature over the range 630–600°C. The difference in Zr activity in these phases may give rise to transport down the temperature gradient. A meaningful analysis of interdiffusion in the two-phase region at the colder end of the rod requires additional information on the thermodynamic and transport properties of the individual phases.

7. Summary

Micro-structural development and constituent redistribution were investigated in rods of a 71U–19Pu–10Zr (wt%) alloy annealed under a temperature gradient of 220°C/cm. The redistribution profiles of U, Pu and Zr observed near the hot end of the sample were analyzed in the framework of multicomponent diffusion under a temperature gradient and concentration gradients of U and Zr. A method based on an integration of interdiffusion fluxes was developed and applied to the concentration profiles of the constituents for the determination of average coefficients of thermotransport (the product of heat of transport and atomic mobility), $\overline{\beta_i \tilde{Q}_i^*}$ and average effective interdiffusion coefficients, $\overline{\tilde{D}}_i^{\text{eff}}$. The diffusion parameters, $\overline{\beta_i \tilde{Q}_i^*}$ and $\overline{\tilde{D}}_i^{\text{eff}}$, for the various components were calculated for selected regions in the diffusion zone. These parameters were employed to estimate the interdiffusion fluxes of U, Pu and Zr. In addition, average values of the ternary interdiffusion coefficients $\overline{\tilde{D}}_{ii}^k$ (main) and $\overline{\tilde{D}}_{ij}^k$ (cross) were also calculated along with the interdiffusion flux contributions arising from the gradients of temperature and concentrations of U and Zr. Appreciable diffusional interactions were identified between Zr and U in the U–Pu–Zr alloys.

Acknowledgements

The diffusion and thermotransport analysis presented in this paper is part of a dissertation submitted by Sohn to Purdue University in partial fulfillment of the requirements for the PhD degree. Grateful appreciation is expressed to Argonne National Laboratory for the financial support.

References

[1] S.R. de Groot, P. Mazur, Non-Equilibrium Thermodynamics, North-Holland, Amsterdam, 1962.
[2] K. Denbigh, The Thermodynamics of Steady State, Methuen's Monographs, London, 1951.
[3] R.A. Oriani, J. Phys. Chem. Solids 30 (1969) 339.
[4] P. Shewmon, Diffusion in Solids, 2nd Ed., TMS, 1989.
[5] J. Philibert, Atom Movements – Diffusion and Mass Transport in Solids, Les Editions de Physique, 1991.
[6] J.R. Manning, Diffusion Kinetics for Atoms in Crystals, D. Van Nostrand, New York, 1968.
[7] G.L. Hofman, S.L. Hayes, M.C. Petri, J. Nucl. Mater. 227 (1996) 277.
[8] W.F. Murphy, W.N. Beck, F.L. Brown, B. Koprowski, L.A. Neimark, Argonne National Laboratory Report, ANL-7602, 1969.
[9] R.G. Pahl, D.L. Porter, C.E. Lahm, G.L. Hofman, Metall. Trans. A 21 (1990) 1063.
[10] D.L. Porter, C.E. Lahm, R.G. Pahl, Metall. Trans. A 21 (1990) 1871.
[11] H. Tsai, L.A. Neimark, Proceedings of the International Conference on Design and Safety of Advanced Nuclear Power Plants, vol. III, session 28, Tokyo, Japan 1992, p. 2.
[12] L. Leibowitz, R.A. Blomquist, A.D. Pelton, J. Nucl. Mater. 167 (1989) 76.
[13] P. Shewmon, Acta Metall. 8 (1960) 605.
[14] D. Jaffe, P.G. Shewmon, Acta Metall. 12 (1964) 515.
[15] M. Uz, D.K. Rehbein, O.N. Carlson, Metall. Trans. A 17 (1986) 1955.
[16] S.C. Axtell, O.N. Carlson, Metall. Trans. A 21 (1990) 2141.
[17] D.P. Campbell, H.B. Huntington, Phys. Rev. 179 (1969) 601.
[18] A. Kirchheim, E. Fromm, Acta Metall. 22 (1974) 1543.
[19] J.G. Shaw, W.A. Oates, Metall. Trans. 2 (1971) 2127.
[20] C.J. Meechan, G.W. Lehman, J. Appl. Phys. 33 (1962) 634.
[21] R.A. McKee, J.P. Stark, Acta Metall. 23 (1975) 1145.
[22] J.D. D'Amico, H.B. Huntington, J. Phys. Chem. Solids 30 (1969) 1697.
[23] M. Kurata, T. Inoue, C. Sari, J. Nucl. Mater. 208 (1994) 144.
[24] D.R. Harbur, J.W. Anderson, W.J. Maraman, Los Alamos Scientific Laboratory Report, LA-4512, 1970.
[25] G.P. Marino, Nucl. Sci. Eng. 49 (1972) 93.
[26] M. Ishida, T. Ogata, M. Kinoshita, Nucl. Technol. 104 (1993) 37.
[27] M.A. Dayananda, Y.H. Sohn, Metall. Mater. Trans. A 30 (1999) 535.
[28] M. Bober, C. Sari, G. Schumacher, J. Nucl. Mater. 39 (1971) 265.
[29] G.L. Hofman, L.C. Walters, in: B.R.T. Frost (Ed.), Nuclear Materials, Part I, vol. 10A VCH; in: R.W Cahn, P. Haasen, E.J. Kramer (Eds.), Materials Science and Technology: A Comprehensive Treatment, VCH, Weinheim, Germany, 1994.

[30] D.R. O'Boyle, A.E. Dwight, Proceedings of the International Conference on Pu and Other Actinide, Santa Fe, NM (1970) Session 2–720.
[31] P.G. Shewmon, Trans. Metall. Soc. AIME 212 (1958) 642.
[32] M.A. Dayananda, C.W. Kim, Metall. Trans. A 10 (1979) 1333.
[33] C.W. Kim, M.A. Dayananda, Metall. Trans. A 14 (1983) 857.
[34] C.W. Kim, M.A. Dayananda, Metall. Trans. A 15 (1984) 649.
[35] M.A. Dayananda, Metall. Trans. A 14 (1983) 1851.
[36] M.A. Dayananda, Mater. Sci. Eng. A 121 (1989) 351.
[37] M.A. Dayananda, D.A. Behnke, Scr. Mater. 25 (1991) 2187.
[38] M.A. Dayananda, Defect Diffusion Forum 95–98 (1993) 521.
[39] M.A. Dayananda, Metall. Trans. A 27 (1996) 2504.
[40] M.A. Dayananda, Y.H. Sohn, Scr. Mater. 35 (1996) 683.
[41] M.C. Petri, M.A. Dayananda, Philos. Mag. 76 (1997) 1169.
[42] M.C. Petri, M.A. Dayananda, J. Nucl. Mater. 240 (1997) 131.